https://doi.org/10.1016/j.ijmachtools.2017.06.004

Feasibility study of the novel quasi-elliptical tool servo for vibration suppression in the turning of micro-lens arrays

Zhiwei Zhu[a], Suet To[b,†], Wu-Le Zhu[c] and Peng Huang[b]

a. School of Mechanical Engineering, Nanjing University of Science and Technology, Nanjing, J.S. 210094, China

b. State Key Laboratory of Ultra-precision Machining Technology, Department of Industrial and Systems Engineering, The Hong Kong Polytechnic University, Kowloon, Hong Kong SAR, China

c. State Key Laboratory of Fluid Power and Mechatronic systems, Zhejiang University, Hangzhou, Z.J. 310027, China

†. Corresponding author: sandy.to@polyu.edu.hk

Abstract

In fast or slow tool servo (F-/STS) diamond turning of micro-lens arrays (MLAs), the inherent non-smooth servo motion will lead to undesired tool vibrations, and it can significantly deteriorate the quality of the machined surface. Starting from a mathematical explanation of the underlying mechanism for vibration suppression, a quasi-elliptical tool servo (QETS) technique and the corresponding optimal toolpath determination algorithm are proposed to overcome the inherent defects in F-/STS turning of MLAs. As for the QETS, the inherent non-smooth servo motion in the F-/STS is proposed to be decomposed into two smooth quasi-harmonic motions along the cutting and servo motion directions, which then constructs the quasi-elliptical trajectory. Taking advantage of the smooth nature of the two decomposed motions, the undesired tool vibrations induced by the motion non-smoothness in the F-/STS can be significantly eliminated, accordingly facilitating the generation of MLAs with homogeneous and smooth surfaces. Finally, the new concept is verified through numerical simulation of the tool motion and experimental demonstration by turning a typical hexagonal aspheric MLA.

Keywords: Ultraprecision diamond turning, slow tool servo, micro-lens array, tool vibration, quasi-elliptical trajectory.

Nomenclature

$[\cdot]$: The round function

$[x_{\mathrm{t}}(j), 0, z_{\mathrm{t}}(j)]$: Coordinate of the j-th point at the tool edge in the global system

$\alpha,\ \beta,\ h,\ m,\ n,\ q$: Integers

Δg : Difference of the term g

Δg_{c} : Velocity of the extra-motion obtained through interpolation

δ : Angular sampling ratio

ϵ : Sampling ratio for tool edge profile discretization

$[x_0, y_0]$: Center point coordinate of a specified lenslet

$\lfloor \cdot \rfloor$: The floor function

$\rho(k)$: Radial position of the k-th CLP

$\rho_{\mathrm{max:}}$ Aperture of the workpiece

θ_0 : Rotational angle with cusp point in the relative acceleration

θ_k : Angular position for the k-th cutting point

φ_n Rotational angle forthe n-th CLP

a_h, b_h, c_h, d_h: Coefficients for the interpolation function

$d_k(j)$: Distance between the j-th point pair at the tool edge and the desired surface

f_{v} : x_{m}-axial feedrate per revolution

g : Extra-motion added along the y-axis direction

$o_{\mathrm{m}} - x_{\mathrm{m}} y_{\mathrm{m}} z_{\mathrm{m}}$: Global coordinate system of the machine tool

$o_{\mathrm{s}} - x_{\mathrm{s}} y_{\mathrm{s}} z_{\mathrm{s}}$: Local coordinate system of a specified lenslet

R_{L} : Aperture of the lenslet

R_{t} : Radius of the diamond tool

$S_{\mathrm{c}}(\cdot)$: The cubic spline interpolation function

$v_\theta,\ a_\theta$: Relative velocity and acceleration with respect to the rotational angle

$x_{\mathrm{c}}, y_{\mathrm{c}}$: x_{m}- and y_{m}-axial motion components induced by the extra-motion g

$X_{\mathrm{m}}, Y_{\mathrm{m}}, Z_{\mathrm{m}}$: x_{m}-, y_{m}-, and z_{m}-axial servo motions in the QETS

$y,\ y_{\mathrm{r}}$: y-axial motions before and after adding the term g, respectively

z_{t} : z_{m} axial coordinate of the tool edge in the global system

z_{v} : The virtual z_{m}-axial position of the CLP

z: z_{m}-axial servo motion in STS

z_{g} : Modified z_{m}-axial servo motion after adding the new term

1. Introduction

Micro-lens arrays (MLAs) are widely used in imaging, illumination, and photoelectric sensor systems due to the fascinating features including miniature size, wide field of view, short processing time, and high sensitivity to motion to mention a few [1–3]. However, the sophisticated structure generally imposes a high challenge on the cost-effective fabrication of MLAs with high surface quality.

Compared with non-traditional fabrication methods, such as self-assembly [4], chemical etching [5], and laser writing [6], the mechanical machining technique is more promising as a generic method for flexible generation of MLAs with complicated shapes, as well as high form accuracy [7]. In general, mechanical machining can be further classified, according to the cutting configuration, into single point diamond milling and diamond turning. As for diamond milling, the rotated tool generates rotationally symmetric lenslets in sequence, accordingly forming the array structure [8, 9]. It can achieve uniform quality of the machined surface well due to the process consistency for cutting each lenslet, but it may also suffer from the common disadvantages of conventional ball-end milling, including low machining efficiency and limited shape complexity of the lenslet [8, 10]. With respect to diamond turning, the fast or slow tool servo (F-/STS) featuring high efficiency and high flexibility is commonly adopted as an outperforming technique for the generation of MLAs. In terms of the structural shape, aspheric or even freeform lenslet can be generated on both planar and curved substrates with the assistance of the oscillation capability of the auxiliary F-/STS system [11–13]. Moreover, by deliberately choosing the cutting parameters, fabrication of a MLA on brittle optical crystals can also be achieved, extending the applicability of F-/STS diamond turning well for a much wider spectrum of engineering materials [14, 15].

Although F-/STS diamond turning is proven to be very promising, the remote quality of the turned surface is highly sensitive to the position of the area on the generated surface, leading to

the inhomogeneity of surface roughness and form accuracy [13, 16, 17]. In spite of the sampling effect in toolpath determination [18, 19] as well as the geometry error of the machine tool [16], the most prominent issue related to the inhomogeneity is the induced vibration of the servo motion in the F-/STS, which is caused by the inevitable non-smooth trajectory adopted in turning a MLA [12, 20]. The motion vibration then prints marks on the machined surface, resulting in deteriorated surface roughness and poor form accuracy [12, 20]. To suppress the vibration induced by non-smooth motion, one potential solution is to slow down the moving velocity, accordingly to constrain the maximum acceleration of the servo motion to be within the dynamic capability of the servo system [21]. Obviously, this may lead to extremely low machining efficiency with high costs. An alternative solution for avoiding the undesired vibration is to virtually construct the rotational axis of the spindle to be through the center of each lenslet. By sequentially shifting the rotational axis, each lenslet can be independently generated as a typical smooth surface through a smooth trajectory. The machined lenslets are finally stitched to be a complete MLA [22]. This process is effective for the generation of very complicated microstructure arrays, but it suffers from low efficiency, low cutting velocity for material removal, and very limited processing area.

As discussed above, although F-/STS diamond turning of MLAs is very promising in terms of cutting efficiency, cutting flexibility, and shape complexity, it is still challenging for the homogeneous generation of lenslets without vibration marks on the machined surface. Motivated by this, a novel quasi-elliptical tool servo (QETS) diamond turning technique is proposed in this paper. By properly decomposing the non-smooth servo motion in the F-/STS into two quasi-harmonic smooth motions, the QETS provides the capability for eliminating the undesired motion vibrations in cutting MLAs well without loss of cutting efficiency.

2. Fast-/slow tool servo turning of MLAs

The configuration of F-/STS diamond turning of a MLA is illustrated in Fig. 1. $o_{\mathrm{m}} - x_{\mathrm{m}} y_{\mathrm{m}} z_{\mathrm{m}}$ is fixed on the spindle and defined as the global coordinate system of the machine tool, where $o_{\mathrm{m}} z_{\mathrm{m}}$ is coincident with the spindle axis. With the generation of a MLA, the common constant angle sampling strategy is employed for the toolpath determination. Assume the angular sampling ratio is δ, the radial position $\rho(k)$ for the k-th cutting point is determined by

$$\rho(k) = \rho_{\max} - \frac{k\delta}{2\pi} f_{\mathrm{v}} \tag{1}$$

where $\rho_{\max}$ denotes the radius of the workpiece, and f_{v} is the feedrate per revolution for the slide motion along the x_{m}-axial direction.

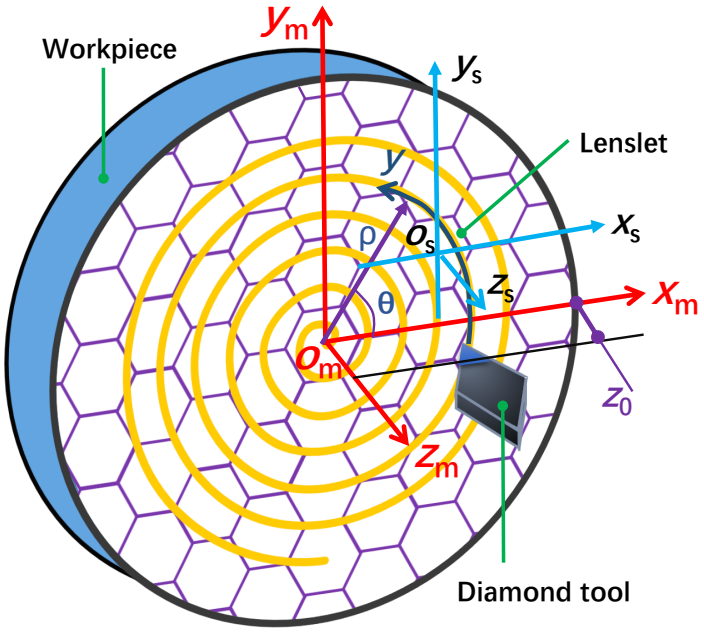

Figure 1: Schematic of the configuration of the turning system.

Assume that a diamond tool with a radius of R_{t} and rake angle of 0 degrees is used for turning, the profile of the cutting edge in the global system $o_{\mathrm{m}} - x_{\mathrm{m}} y_{\mathrm{m}} z_{\mathrm{m}}$ can be expressed by [22]

$$z_{\mathrm{t}}(k) = z_{\mathrm{v}} + R_{\mathrm{t}} - \sqrt{R_{\mathrm{t}}^2 - [x_{\mathrm{m}} - \rho(k)]^2} \tag{2}$$

where $x_{\mathrm{m}} \in [\rho(k) - R_{\mathrm{t}}, \rho(k) + R_{\mathrm{t}}]$, and z_{v} represents the virtual position of the cutter location point (CLP) along the z_{m}-axial direction as shown in Fig. 1.

Assume that $o_{\mathrm{s}} - x_{\mathrm{s}}y_{\mathrm{s}}z_{\mathrm{s}}$ is defined as the local coordinate system of each lenslet with z_{s} axis parallel to the spindle axis. It is attached at the center of each lenslet in a MLA, and it will rotate with the spindle. Therefore, the shape of each lenslet can be described in its local coordinate system as $z_{\mathrm{s}} = S(x_{\mathrm{s}}, y_{\mathrm{s}})$. Considering the rotation of the spindle, the projected profile of the tool edge on the desired surface along the z_{m}-axial direction can be determined in the global system $o_{\mathrm{m}} - x_{\mathrm{m}}y_{\mathrm{m}}z_{\mathrm{m}}$ as

$$z_{\mathrm{s}}(k) = S\left(x_{\mathrm{m}} \cos\theta_k - x_0, x_{\mathrm{m}} \sin\theta_k - y_0\right) \tag{3}$$

where $\theta_k = k\delta$, and $[x_0, y_0]$ is the coordinate of the center point o_{s} of the corresponding lenslet as shown in Fig. 1.

For a hexagonal MLA, the intervals between any two successive lenslets along the x_{m}- and y_{m}-axial directions are about $\frac{3}{2}R_{\mathrm{L}}$ and $\frac{\sqrt{3}}{2}R_{\mathrm{L}}$, respectively. From the geometric relationships between the lenslets, coordinates of the center point o_{s} of the lenslet under cut can be determined by

$$x_0 = \frac{3}{2}\alpha R_{\mathrm{L}} \tag{4}$$

$$y_0 = \sqrt{3}\beta R_{\mathrm{L}} - \frac{\sqrt{3}}{2}\left(\alpha - 2\lfloor\frac{\alpha}{2}\rfloor\right) R_{\mathrm{L}} \tag{5}$$

where $\lfloor\cdot\rfloor$ is the floor function, which returns the greatest integer less than or equal to the number being processed. $\alpha = \lfloor\frac{2|x_{\mathrm{m}}\cos\theta_k|}{3R_{\mathrm{L}}}\rfloor$, and $\beta = \lfloor\frac{|x_{\mathrm{m}}\sin\theta_k|}{\sqrt{3}R_{\mathrm{L}}}\rfloor$, denoting the relative position of the lenslets in a MLA. R_{L} stands for the radius of each lenslet.

To accurately generate the desired shape of the machined surface, the cutter contact point (CCP) is defined as the point at the tool edge, where the tool edge is tangential to the desired surface. To numerically find the CCP, the tool edge profile is equally discretized by a sampling ratio of ϵ along the x_{m}-axial direction. With an arbitrary point (the j-th point for example) at the tool edge, the distance $d_k(j)$ between this point and the corresponding projection point on the desired surface can be expressed by:

$$\begin{cases} d_k(j) = |z_{\mathrm{s}}(k) - z_{\mathrm{t}}(k)|_{x_{\mathrm{m}}=x_{\mathrm{t}}(j)} \\ x_{\mathrm{t}}(j) = \rho(k) - R_{\mathrm{t}} + j \cdot \epsilon \end{cases} \tag{6}$$

Practically, when the diamond tool is approaching the desired surface along the z_{m}-axial direction as illustrated in Fig. 1, the CCP will firstly contact the surface. This suggests that the distance between the CCP and the corresponding projection point is the minimum one [22]. Therefore, the required servo motion along the z_{m}-axial direction can be determined by $z(k) = \min(d_k)$. Essentially, F-/STS diamond turning is a tri-axial cutting operation, and the term $\rho(k)$ and $z(k)$ are realized by the x_{m}-axial and z_{m}-axial motions, respectively. Meanwhile, the term θ_k is implemented by the rotation of the spindle. Taking the spindle rotation as the motion reference, the servo motion $z(k)$ can be regarded as a function of the angle θ_k, namely $z(k) = f_{\mathrm{c}}(\theta_k)$.

To characterize the features of the toolpath in the turning of MLAs, a typical hexagonal MLA with the derived spiral toolpath is illustrated in Fig. 2. The enlarged view of the servo motion z is shown in Fig. 3 (a), featuring sharp and non-smooth cusps. The corresponding velocity $v_\theta = \frac{\mathrm{d}z}{\mathrm{d}\theta}$ and acceleration $a_\theta = \frac{\mathrm{d}^2 z}{\mathrm{d}\theta^2}$ with respect to the rotational angle θ are further shown in Figs. 3 (b) and 3 (c), respectively. As for the velocity v_θ, a sudden change of the moving direction is observed corresponding to the cusp point at the servo motion z, which further leads to a abrupt change with a large value for the acceleration a_θ as shown in Fig. 3 (c). In general, the relatively large acceleration

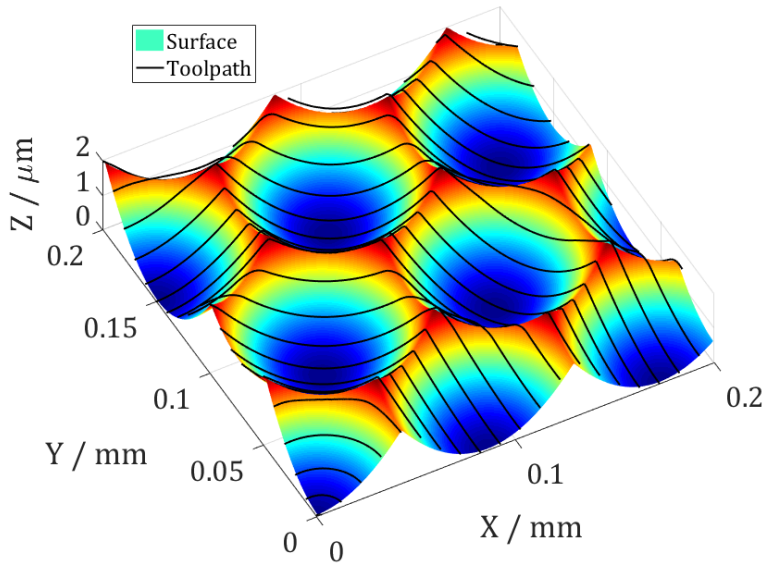

Figure 2: A typical hexagonal MLA with the corresponding toolpath.

may exceed the dynamic capability of the moving axis executing the servo motion, leading to the undesired vibration of the moving axis along the z_{m}-axial direction of the machine tool.

3. Quasi-elliptical tool servo

The newly proposed QETS diamond turning technique adopts the same configuration as that used in F-/STS, which is illustrated in Fig. 1. The difference for the QETS lies in the decomposition of the non-smooth z_{m}-axial servo motion in the F-/STS into two quasi-harmonic motions along the cutting and z_{m}-axial directions. Therefore, a quasi-elliptical trajectory is constructed in the QETS. More details of the principle for vibration suppression and the corresponding toolpath determination strategy are discussed as follows.

3.1. Principle for vibration suppression

By defining a coordinate axis y along the cutting direction as illustrated in Fig. 1, the relative motion of the tool induced by the rotation of the spindle can be derived by $y(\theta) = \rho\theta$. Therefore, considering the two parametric equations $y(\theta)$ and $z(\theta)$, the following relationship for the relative

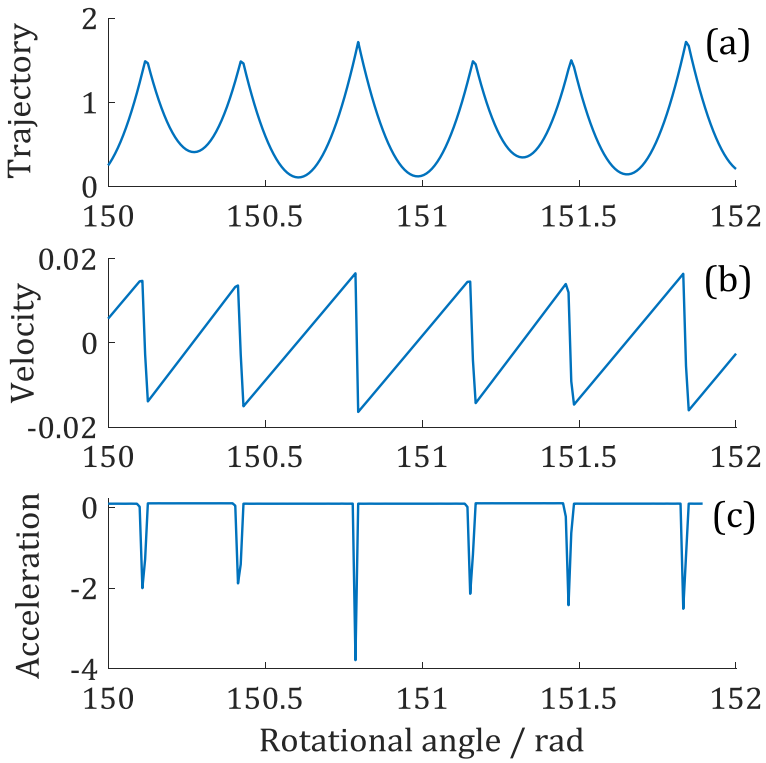

Figure 3: Schematic of (a) the trajectory, (b) the velocity, and (c) the acceleration of the servo motion with respect to the rotation angle θ, and the units are μm, mm/rad, and mm/rad^2, respectively.

motion $z = f(y)$ between the diamond tool and the workpiece can be obtained

$$\frac{\partial z}{\partial y} = \frac{\partial z}{\partial \theta} \cdot \left(\frac{\partial y}{\partial \theta}\right)^{-1} \tag{7}$$

For the turning, the relative velocity of the cutting motion along the y-axial direction can be expressed with respect to the angle θ by

$$\frac{\partial y}{\partial \theta} = \rho_{\max} - \frac{\theta}{2\pi} f_{\mathrm{v}}, \ \theta \leq \frac{2\pi\rho_{\max}}{f_{\mathrm{v}}} \tag{8}$$

This suggests that the relative velocity is linearly dependent on the angle θ. Meanwhile, from the relationship shown in Eq. (7) and Eq. (8), the non-smoothness in the relative motion $z = f(y)$ between the diamond tool and the workpiece will be inherently reserved for the servo motion $z(\theta)$.

For a specified MLA, the relative motion $z = f(y)$ between the diamond tool and the workpiece is unchangeable to construct the desired surface. However, to avoid the non-smooth servo motion $z(\theta)$ as shown in Fig. 3 (a), the relationship in Eq. (7) can be modified by adding an extra-motion $g(\theta)$ to $y(\theta)$, which yields

$$\frac{\partial z_{\mathrm{g}}}{\partial \theta} = \frac{\partial z}{\partial y} \cdot \left(\frac{\partial y}{\partial \theta} + \frac{\partial g}{\partial \theta} \right) \tag{9}$$

With an arbitrary angle $\theta = \theta_0$ at which the cusp point appears as shown in Fig. 3, the newly introduced term $g(\theta)$ should satisfy the following relationship to eliminate the abrupt change of the relative velocity for the servo motion $z(\theta)$

$$\left(\frac{\partial y}{\partial \theta} + \frac{\partial g}{\partial \theta} \right) \Big|_{\theta=\theta_0} = 0 \tag{10}$$

Although the non-smoothness still occurs for the relative motion $z = f(y)$, the term $g(\theta)$ can guarantee a continuous servo motion z_{g} along the z_{m}-axial direction, attributing to the multiplication of the velocity by a factor of 0 as described in Eq. (9) and Eq. (10).

3.2. Toolpath determination for the QETS

Without loss of generality, assume that two successive cusps are the h-th and $(h+m)$-th points in the toolpath series $z(\theta)$. To satisfy Eq. (10), the following numerical relationship for the two cusp points are required

$$\Delta g(h) = \frac{g(h) - g(h-1)}{\delta} = -\frac{\delta h}{2\pi} f_{\mathrm{v}} + \rho_{\max} \tag{11}$$

$$\Delta g(h+m) = \frac{g(h+m) - g(h+m-1)}{\delta} = -\frac{\delta (h+m)}{2\pi} f_{\mathrm{v}} + \rho_{\max} \tag{12}$$

With the increase of the number h, the velocity will decrease towards zero considering the constraint as given in Eq. (8). This suggests that the tool should continuously move along one

direction. In general, it is impossible for the machine tool to implement such motion in cutting. To practically realize the relationship shown in Eq. (11) and Eq. (12), a constraint of the moving direction of the tool is proposed by setting the velocity at a point between the two cusps along the opposite direction, namely

$$\Delta g(q) = \frac{g(q) - g(q-1)}{\delta} = \frac{q\delta}{2\pi} f_{\mathrm{v}} - \rho_{\max},\ q = h + \left[\frac{m}{2}\right] \tag{13}$$

where $[\cdot]$ is the round function which rounds the processed number to the nearest integer.

For the n-th point in the velocity series with $n \in [h, q]$, the corresponding velocity $\Delta g_{\mathrm{c}}(n)$ can be smoothly obtained by adopting the cubic spline interpolation, which yields:

$$\Delta g_{\mathrm{c}}(n) = a_h(\theta_n - \theta_h)^3 + b_h(\theta_n - \theta_h)^2 + c_h(\theta_n - \theta_h) + d_h \tag{14}$$

where $\theta_n = n\delta$, $\theta_h = h\delta$, and the four coefficients a_h, b_h, c_h and d_h can be solved by combining $\Delta g_{\mathrm{c}}(h) = \Delta g(h)$, $\Delta g_{\mathrm{c}}(q) = \Delta g(q)$, $\Delta \dot{g}_{\mathrm{c}}(h) = \Delta \dot{g}(h)$, and $\Delta \ddot{g}_{\mathrm{c}}(q) = \Delta \ddot{g}(q)$. Accordingly, Eq. (14) can be simplified to

$$\Delta g_{\mathrm{c}}(n) = a_h(n-h)^3\delta^3 + b_h(n-h)^2\delta^2 + c_h(n-h)\delta + d_h \tag{15}$$

Therefore, the newly introduced term $g(n)$ can be reconstructed as

$$g(n) = \delta \Delta g_{\mathrm{c}}(n) + g(n-1) \tag{16}$$

Considering the zero initial conditions, i.e. $g(1) = 0$, the motion term g can be iteratively obtained from Eq. (16). Furthermore, combining Eq. (8), the motion of the diamond tool relative

to the workpiece along the cutting direction, i.e., the y-axial direction, becomes

$$y_{\mathrm{r}}(n) = \int_0^{\theta_n} \left(\frac{\partial y}{\partial \theta} + \frac{\partial g}{\partial \theta} \right) \mathrm{d}\theta = n\delta \left(\rho_{\max} - \frac{n\delta}{2\pi} f_{\mathrm{v}} \right) + g(n) \tag{17}$$

Based on the original toolpath as discussed in Section 2, the relationship between the two motions $z(\theta)$ and $y(\theta)$ can be constructed through the cubic spline interpolation function as $z = S_{\mathrm{c}}(y)$ with $S_{\mathrm{c}}(\cdot)$ standing for the cubic spline interpolation function. Therefore, by replacing y with y_{r}, the modified servo motion along the z_{m}-axis can be accordingly obtained as $Z_{\mathrm{m}} = S_{\mathrm{c}}(y_{\mathrm{r}})$. Since the motion term g is designed along the cutting direction, namely the y-axial direction, it will be implemented by combining the x_{m}- and y_{m}-axial servo motions of the machine tool. The required two motion components yield

$$\begin{cases} x_{\mathrm{c}}(n) = \rho(n)\,(1 - \cos\varphi_n) \\ y_{\mathrm{c}}(n) = \rho(n) \sin\varphi_n \end{cases} \tag{18}$$

with

$$\varphi_n = \arctan\left[\frac{g(n)}{\rho(n)}\right] = \arctan\left[\frac{2\pi g(n)}{2\pi\rho_{\max} - n\delta f_{\mathrm{v}}}\right] \tag{19}$$

For practical cutting, Z_{m} is implemented by the moving axis along the z_{m}-axial direction. Meanwhile, $Y_{\mathrm{m}} = y_{\mathrm{c}}$ and $X_{\mathrm{m}} = x_{\mathrm{c}} + \rho$ are implemented by the moving axes along the y_{m}- and x_{m}-axial directions of the machine tool, respectively. Considering the two quasi-harmonic oscillations Z_{m} and g, it mainly forms the quasi-elliptical trajectory for the relative motions between the diamond tool and the workpiece. Therefore, it can be properly called the *Quasi − Elliptical Tool Servo* (QETS) technique.

4. Experimental results and discussion

To realize the proposed QETS diamond turning which requires oscillations motion along the three translational directions, a four-axis ultra-precision machine tool (350 FG, Moore Nanotech Inc., USA) was employed in this research. A natural diamond tool from Contour Fine Tooling Inc. (UK) with a 0.103 mm nose radius and zero rake angle was adopted. The practical hardware configuration is illustrated in Fig. 4 (a), and an enlarged view of the interaction between the diamond tool and the workpiece during turning is further given in Fig. 4 (b). For comparison, generation of MLAs through the conventional STS diamond turning was also conducted. With both the STS and QETS, the spindle speed and feedrate were kept the same, i.e. 15 rpm and 5 μm/rev, respectively.

After cutting, the three-dimensional (3-D) micro-topography of the surfaces generated by both the STS and QETS was captured by an Optical Surface Profiler (Nexview, Zygo Corporation, USA). The vibration marks on the surface were then detracted by removing the best-fitted curved shape from the single lenslet through the analysis software Mx^{TM} from Zygo corporation.

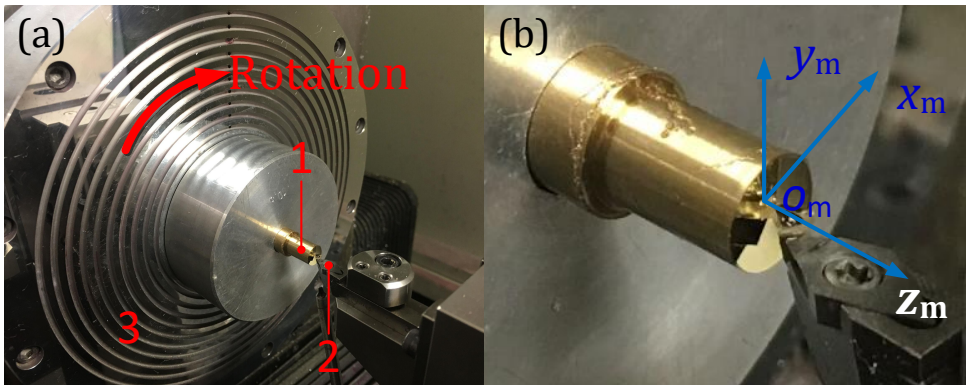

Figure 4: Hardware configuration of the practical cutting system, (a) the global view, and (b) the enlarged view of the interaction between the diamond tool and the workpiece, where 1. the workpiece, 2. the diamond tool, 3. the spindle.

4.1. Characteristics of the toolpath

A hexagonal aspheric MLA was fabricated for experimental demonstration. The height and diameter of each lenslet were 2 μm and 100 μm, respectively. Details of the mathematical description of each lenslet can be found in Ref. [15]. The radius of the machined surface was $\rho_{\max} = 1.5$ mm. For the conventional STS diamond turning, the required servo motions with cutting position at $\rho = 1.101$ mm is illustrated with respect to the defined coordinate $y = \rho\theta$ in Fig. 5 (a). By introducing the auxiliary motion g along the cutting direction in the QETS, the resulting modified servo motions Z_{m} and g along the z_{m}- and y-axial directions are shown in Figs. 5 (b) and 5 (c), respectively. In addition, the reconstructed relative motion between the diamond tool and the workpiece, namely the term Z_{m} with respect to the term y_{r}, is also illustrated in Fig. 5 (a), showing good agreement with that used in the STS. To give a comprehensive evaluation of the toolpath at different cutting positions, the servo motion, Z_{m}, and g at $\rho = 0.372$ mm are further illustrated in Figs. 5 (d), (e) and (f), and the corresponding relationship between Z_{m} and y_{r} is also shown in Fig. 5 (d).

From the results shown in Fig. 5, both the required servo motions g and Z_{m} in the QETS appear to be harmonic-like and smooth without any sharp cusps. The reconstructed diagrams showing the relationships between the two terms g and Z_{m} at $\rho = 1.101$ mm and $\rho = 0.372$ mm are further illustrated in Figs. 6 (a) and (b), respectively, which represent the relative trajectory of the servo motions imposed on the diamond tool and the workpiece. Obviously, the inherent closed loop trajectory with varying shape shows a quasi-elliptical feature at each cutting position, demonstrating that a quasi-elliptical motion is employed in the QETS turning.

Furthermore, as for the cutting position at $\rho = 1.101$ mm, the velocities and accelerations of the servo motions along the z_{m}-axial adopted in both the STS and QETS are compared in Figs. 7 (a) and (b), and the velocities and accelerations of the servo motions at $\rho = 0.372$ mm are further

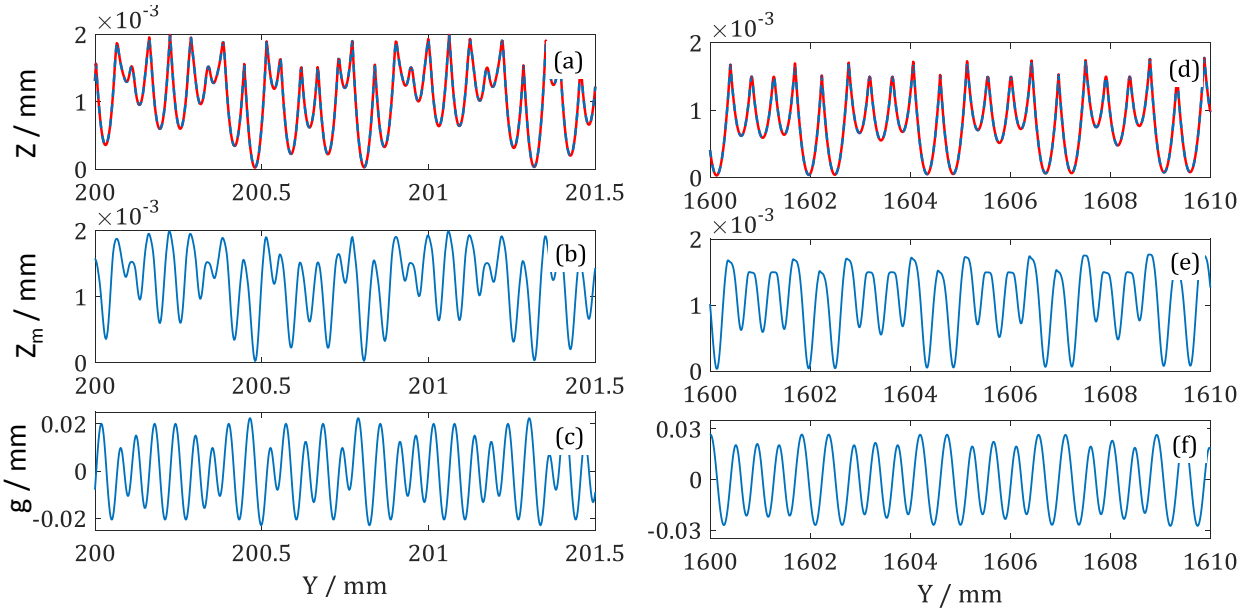

Figure 5: Characteristics of the tool trajectories for both the STS and QETS with respect to the defined y-axis at position (a) $\rho = 1.101$ mm, and (d) $\rho = 0.372$ mm; the servo motion along the z_{m}-axis for the QETS at (b) $\rho = 1.101$ mm, and (e) $\rho = 0.372$ mm; motion of the newly introduced term g at (c) $\rho = 1.101$ mm, and (f) $\rho = 0.372$ mm.

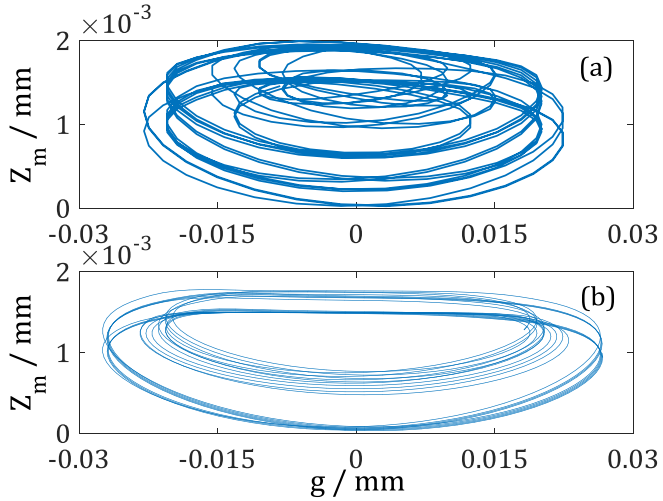

Figure 6: Relationship between the two terms g and Z_{m} at (a) $\rho = 1.101$ mm, and (b) $\rho = 0.372$ mm.

illustrated in Figs. 7 (c) and (d). Similar to that shown in Fig. 3 (b) and Fig. (3) (c), sudden changes of the moving direction, as well as the corresponding abrupt changes of the acceleration are observed for the servo motion used in the STS as illustrated in Fig. 7. However, by superimposing the new term g along the cutting direction in the QETS, the velocity for the modified servo motion along the z_{m}-axial direction appears to be smooth without sudden changes. Furthermore, the

corresponding acceleration exhibits a smooth quasi-harmonic feature, and varies periodically along the forward and backward directions. This suggests that the non-smooth servo motion along the z_{m}-axial direction in the STS is decomposed well into two quasi-harmonic smooth motions in the y and z_{m}-axial directions in the QETS.

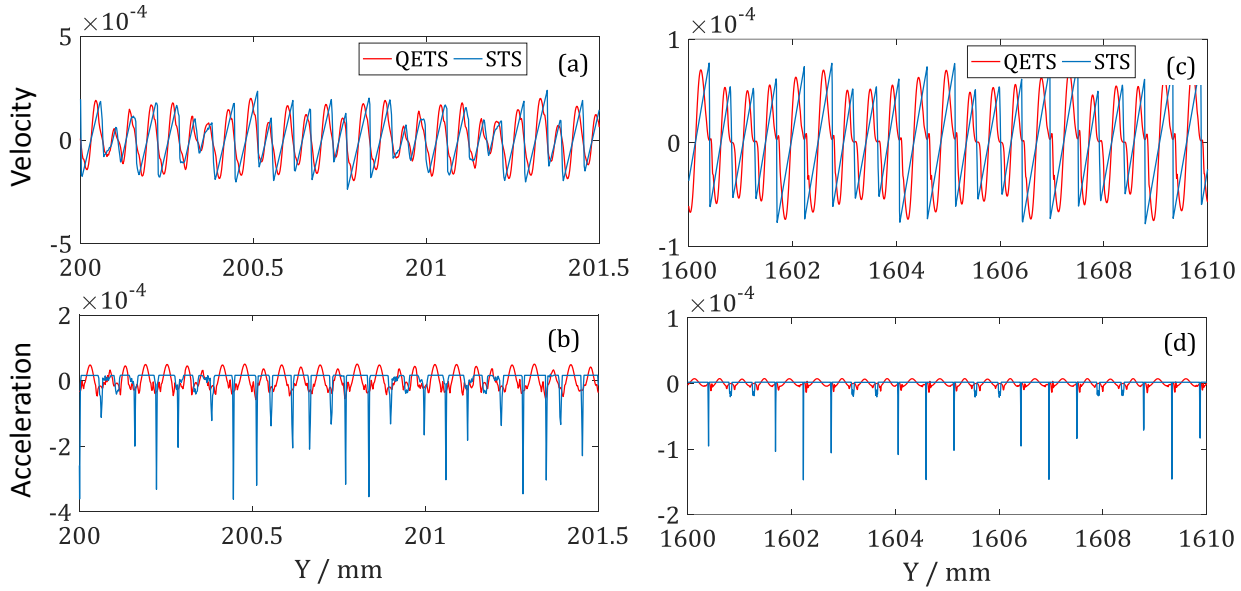

Figure 7: Comparison of (a) the velocity, and (b) the acceleration of the servo motions for the STS and QETS at $\rho = 1.101$ mm; and (c) the velocity, and (d) the acceleration of the servo motions at $\rho = 0.372$ mm.

4.2. Characteristics of surface micro-topography

As discussed in Section 2.1, the vibration of the machine tool is caused by the over-large acceleration, so the characteristics of the induced vibration marks on the machined surface will be highly dependent on the cutting velocity, namely the relative distance from the rotational center of the spindle. Therefore, for the two samples generated by the STS and QETS, three lenslets with relative distances of about 1.45 mm, 0.8 mm and 0.25 mm to the rotational center were investigated. To avoid repetition, only the detracted micro-topographies with removal of the best fitted curved shapes are illustrated in Fig. 8. The three regions are labeled as far (F), medial (M) and close (C) for the convenience of the following discussions.

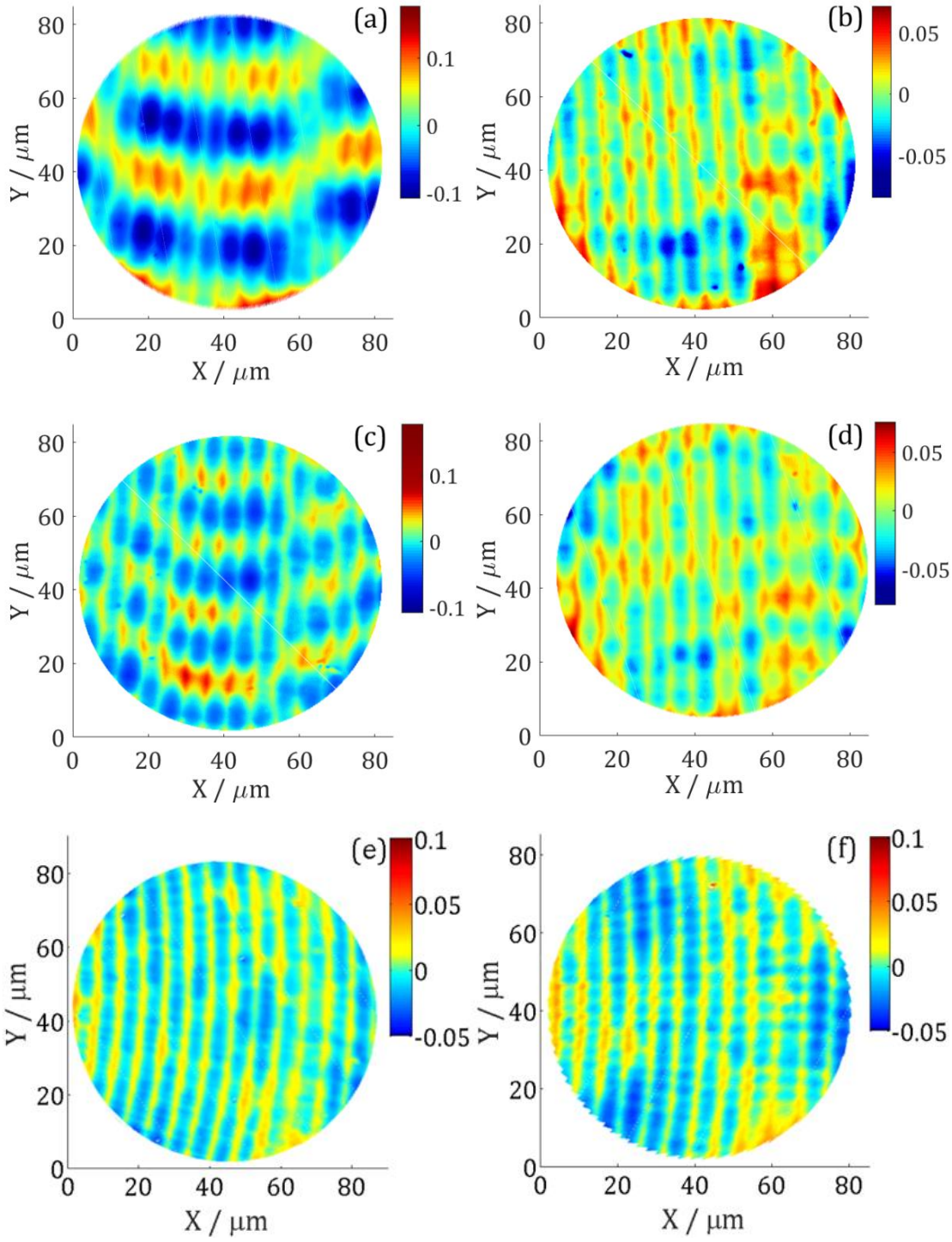

Figure 8: The detracted surface micro-topographies of the far lenslets generated by (a) the STS and (b) the QETS, the medial lenslets generated by (c) the STS and (d) the QETS, and the close lenslets generated by (e) the STS and (f) the QETS.

As shown in Figs. 8 (a) and 8 (c), the detracted micro-topographies generated by the STS exhibit periodic fluctuations with different spatial frequencies along the cutting direction, together with the irregular residual tool marks along the side-feeding direction. When the lenslet is very close to the center, namely the velocity is very small, the micro-topography in Fig. 8 (e) exhibits a relatively smooth feature with slight fluctuations at the scale of several nanometers. In contrast, with the surface generated by the QETS, the detracted micro-topographies for the lenslets in the far and medial regions have similar features as shown in Figs. 8 (b) and 8 (d), and the surfaces are free of strong fluctuations along the cutting direction. However, the residual tool marks along the side-feeding direction appear to be a bit irregular, suggesting that the diamond tool suffers from slight vibrations. The micro-topography in Fig. 8 (f) shows much more regular residual tool marks with intensive dots along the cutting direction, which is similar to that in Fig. 8 (e). The results demonstrate that the proposed QETS diamond turning can significantly eliminate the undesired vibrations compared with the STS, especially for cutting at high velocity.

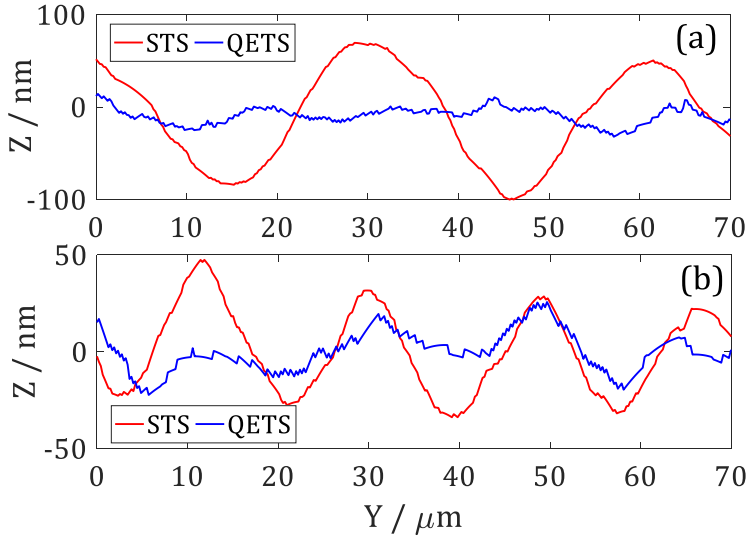

Figure 9: The cross-sectional profiles for (a) the far lenslets, and (b) the medial lenslets.

Since the topographical features are similar for regions close to the center, only the cross-sectional profiles for surfaces shown in Figs. 8 (a) 8 (d) are illustrated in Fig. 9, which are captured along

the cutting direction. The peak to valley (PV) values for the fluctuations generated by the STS are about 169.7 nm and 75.1 nm with respect to the lenslets in the far and medial regions. As for the far region, the cutting velocity is relatively higher than that in the medial region when subjected to a constant spindle speed. Therefore, the vibration amplitude of the machine tool in the far region will be much larger, resulting in the larger PV value of the fluctuations on the machined surface. Regarding the other aspect, the corresponding PV values for the QETS are about 36.9 nm and 40.1 nm. This further suggests that the proposed QETS is effective in relation to the elimination of the undesired tool vibrations in the turning of MLAs.

In addition, the surface roughness (Sa) for each lenslet in the far, medial, and close regions as illustrated in Fig. (8) is identified through the analysis software of the optical profiler. To investigate the consistency of the quality of the machined surface, roughness of the mentioned lenslet in each region together with the other six surrounding it was measured and statistically analyzed, leading to the mean, variance, and maximum values for all the regions summarized in Table 1. In general, it suggests that highly consistent roughness for the surface in each region is achieved. As for the surface generated by the STS, it indicates that the mean roughness is highly dependent on the relative distance of the region to the rotational center which directly relates with the cutting velocity, and better surface quality is obtained for the surface in the region closer to the rotational center.

As for the roughness of the surface generated by the QETS, the mean roughness for surfaces in the far and medial regions was about 13.73 nm and 14.02 nm, respectively, demonstrating very slight dependence on the relative distance. Moreover, compared with the roughness for the STS turned surfaces in the two regions, namely 40.24 nm and 19.07 nm, significant improvement was realized through the QETS technique. In accordance with the observations in Figs. 8 (e) and (f), surfaces in the close regions generated by both the STS and QETS exhibited similar quality in

terms of the mean and maximum roughness. Overall, this suggests that the QETS is capable of the generation of MLAs with homogeneous quality irrespective of the position of the lenslets.

Table 1: Summary of surface roughness, unit nm.

	STS			QETS		
	F	M	C	F	M	C
Mean	40.24	19.07	10.48	13.73	14.02	10.70
Max	42.88	19.75	11.14	14.41	14.46	11.18
Var	4.77	0.22	0.36	0.26	0.14	0.17

5. Conclusion

A quasi-elliptical tool servo (QETS) diamond turning technique is proposed for the generation of micro-lens arrays (MLAs). Compared with the conventional fast-/slow tool servo (F-/STS), an extra servo motion is introduced along the cutting direction in the QETS. Therefore, the inevitable non-smooth motion used in F-/STS diamond turning of MLAs is decomposed well into two smooth quasi-harmonic motions in the QETS. This leads to the elimination of the undesired tool vibrations induced by the non-smooth motion in the F-/STS, providing the QETS with the capability of the generation of high quality MLAs without loss of machining efficiency.

Practically, the decomposition algorithm for the determination of the optimal toolpath in the QETS was developed with further discussion of the motion characteristics. Experimental turning of a typical hexagonal aspheric MLA was conducted through both the STS and QETS techniques, and the resulting surfaces were measured and statistically analyzed as a comparative study. The comparison results of surface roughness in different regions indicate that the surface generated by the QETS is of high homogeneity and free of strong fluctuations which occur on the surface generated by the STS. The result demonstrates the effectiveness and superiority of the proposed QETS for the generation of MLAs well.

Acknowledgments

This work is jointly supported by the Fundamental Research Funds for the Central Universities (30917011301), and the National Natural Science Foundation of China (51675455).

References

[1] Y. M. Song, Y. Xie, V. Malyarchuk, J. Xiao, I. Jung, K.-J. Choi, Z. Liu, H. Park, C. Lu, R.-H. Kim, et al., Digital cameras with designs inspired by the arthropod eye, Nature 497 (7447) (2013) 95–99.

[2] Z. Deng, F. Chen, Q. Yang, H. Bian, G. Du, J. Yong, C. Shan, X. Hou, Dragonfly-eye-inspired artificial compound eyes with sophisticated imaging, Advanced Functional Materials 26 (12) (2016) 1995–2001.

[3] K. Pang, L. Song, F. Fang, Y. Zhang, H. Zhang, An imaging system with a large depth of field based on an overlapped micro-lens array, CIRP Annals-Manufacturing Technology 65 (1) (2016) 471–474.

[4] K. Lee, W. Wagermaier, A. Masic, K. P. Kommareddy, M. Bennet, I. Manjubala, S.-W. Lee, S. B. Park, H. Cölfen, P. Fratzl, Self-assembly of amorphous calcium carbonate microlens arrays, Nature communications 3 (2012) 725.

[5] H. Bian, Y. Wei, Q. Yang, F. Chen, F. Zhang, G. Du, J. Yong, X. Hou, Direct fabrication of compound-eye microlens array on curved surfaces by a facile femtosecond laser enhanced wet etching process, Applied Physics Letters 109 (22) (2016) 221109.

[6] Z. Deng, Q. Yang, F. Chen, X. Meng, H. Bian, J. Yong, C. Shan, X. Hou, Fabrication of large-area concave microlens array on silicon by femtosecond laser micromachining, Optics letters 40 (9) (2015) 1928–1931.

[7] F. Fang, X. Zhang, A. Weckenmann, G. Zhang, C. Evans, Manufacturing and measurement of freeform optics, CIRP Annals-Manufacturing Technology 62 (2) (2013) 823–846.

[8] B. McCall, T. S. Tkaczyk, Rapid fabrication of miniature lens arrays by four-axis single point diamond machining, Optics express 21 (3) (2013) 3557–3572.

[9] S. Kirchberg, L. Chen, L. Xie, G. Ziegmann, B. Jiang, K. Rickens, O. Riemer, Replication of precise polymeric microlens arrays combining ultra-precision diamond ball-end milling and micro injection molding, Microsystem technologies 18 (4) (2012) 459–465.

[10] J. Yan, Z. Zhang, T. Kuriyagawa, H. Gonda, Fabricating micro-structured surface by using single-crystalline diamond endmill, The International Journal of Advanced Manufacturing Technology 51 (9-12) (2010) 957–964.

[11] L. Li, Y. Y. Allen, Design and fabrication of a freeform microlens array for a compact large-field-of-view compound-eye camera, Applied optics 51 (12) (2012) 1843–1852.

[12] S. Scheiding, Y. Y. Allen, A. Gebhardt, L. Li, S. Risse, R. Eberhardt, A. Tünnermann, Freeform manufacturing of a microoptical lens array on a steep curved substrate by use of a voice coil fast tool servo, Optics express 19 (24) (2011) 23938–23951.

[13] Y.-L. Chen, S. Wang, Y. Shimizu, S. Ito, W. Gao, B.-F. Ju, An in-process measurement method for repair of defective microstructures by using a fast tool servo with a force sensor, Precision Engineering 39 (2015) 134–142.

[14] M. Mukaida, J. Yan, Ductile machining of single-crystal silicon for microlens arrays by ultra-precision diamond turning using a slow tool servo, International Journal of Machine Tools and Manufacture 115 (2017) 2–14.

[15] D. Yu, Y. Wong, G. Hong, Ultraprecision machining of micro-structured functional surfaces on brittle materials, Journal of micromechanics and microengineering 21 (9) (2011) 095011.

[16] X. Liu, X. Zhang, F. Fang, Z. Zeng, H. Gao, X. Hu, Influence of machining errors on form errors of microlens arrays in ultra-precision turning, International Journal of Machine Tools and Manufacture 96 (2015) 80–93.

[17] L. Kong, C. Cheung, Modeling and characterization of surface generation in fast tool servo machining of microlens arrays, Computers & Industrial Engineering 63 (4) (2012) 957–970.

[18] D. W. K. Neo, A. S. Kumar, M. Rahman, A novel surface analytical model for cutting linearization error in fast tool/slow slide servo diamond turning, Precision engineering 38 (4) (2014) 849–860.

[19] Z. Zhu, S. To, Adaptive tool servo diamond turning for enhancing machining efficiency and surface quality of freeform optics, Optics express 23 (16) (2015) 20234–20248.

[20] Z. Zhu, S. To, S. Zhang, Large-scale fabrication of micro-lens array by novel end-fly-cutting-servo diamond machining, Optics express 23 (16) (2015) 20593–20604.

[21] E. Brinksmeier, R. Gläbe, L. Schönemann, Diamond micro chiseling of large-scale retroreflective arrays, Precision Engineering 36 (4) (2012) 650–657.

[22] S. To, Z. Zhu, H. Wang, Virtual spindle based tool servo diamond turning of discontinuously structured microoptics arrays, CIRP Annals-Manufacturing Technology 65 (1) (2016) 475–478.

List of Figures

Figure 1 Schematic of the configuration of the turning system.

Figure 2 A typical hexagonal MLA with the corresponding toolpath.

Figure 3 Schematic of (a) the trajectory, (b) the velocity, and (c) the acceleration of the servo motion with respect to the rotation angle θ, and the units are μm, mm/rad, and mm/rad^2, respectively.

Figure 4 Hardware configuration of the practical cutting system, (a) the global view, and (b) the enlarged view of the interaction between the diamond tool and the workpiece, where 1. the workpiece, 2. the diamond tool, 3. the spindle.

Figure 5 Characteristics of the tool trajectories for both the STS and QETS with respect to the defined y-axis at position (a) $\rho = 1.101$ mm, and (d) $\rho = 0.372$ mm; the servo motion along the z_{m}-axis for the QETS at (b) $\rho = 1.101$ mm, and (e) $\rho = 0.372$ mm; motion of the newly introduced term g at (c) $\rho = 1.101$ mm, and (f) $\rho = 0.372$ mm.

Figure 6 Relationship between the two terms g and Z_{m} at (a) $\rho = 1.101$ mm, and (b) $\rho = 0.372$ mm.

Figure 7 Comparison of (a) the velocity, and (b) the acceleration of the servo motions for the STS and QETS at $\rho = 1.101$ mm; and (c) the velocity, and (d) the acceleration of the servo motions at $\rho = 0.372$ mm.

Figure 8 The detracted surface micro-topographies of the far lenslets generated by (a) the STS and (b) the QETS, the medial lenslets generated by (c) the STS and (d) the QETS, and the close lenslets generated by (e) the STS and (f) the QETS.

Figure 9 The cross-sectional profiles for (a) the far lenslets, and (b) the medial lenslets.

List of Tables

Table 1 Summary of surface roughness, unit nm.